



Estimation of solar direct beam transmittance of conifer canopies from airborne LiDAR



Keith N. Musselman^{a,b,*}, Steven A. Margulis^a, Noah P. Molotch^{b,c}

^a Department of Civil and Environmental Engineering, 5732 Boelter Hall, Box 951593, University of California, Los Angeles, CA 90095-1593, USA

^b Institute of Arctic and Alpine Research and Department of Geography, 1560 30th Street, 450 UCB, University of Colorado, Boulder, CO, 80309-0450, USA

^c Jet Propulsion Laboratory, California Institute of Technology, Pasadena, CA 91109, United States

ARTICLE INFO

Article history:

Received 3 January 2013

Received in revised form 11 May 2013

Accepted 25 May 2013

Available online 21 June 2013

Keywords:

Forest canopy

LiDAR

Voxel model

Ray-tracing

Solar direct beam radiation

ABSTRACT

The utility of airborne scanning LiDAR data to estimate solar direct beam canopy transmittance in complex, forested terrain was evaluated. Twenty-four hemispherical photos were used to produce ground-based estimates of solar direct beam canopy transmittance. The photo estimates were used to develop and evaluate two spatially distributed canopy transmittance models: 1) a Beer's Law-type transmittance model based on LiDAR-derived canopy metrics, and 2) a solar raytrace model applied to a three-dimensional canopy model. The models were used to estimate solar direct beam canopy transmittance at five-minute resolution for all days between the winter and summer solstices over an 800 m by 700 m domain at 1 m horizontal grid spacing. When compared to estimates from hemispherical photos, the raytrace model resolved the complex seasonal and diurnal variability of solar direct beam canopy transmittance resulting from individual trees and localized canopy structure. The Beer's-type model was unable to resolve these detailed factors. The two models exhibited similar and relatively low normalized daily mean error values from December to early March. Later in the season (01 March–21 June), the model differences were pronounced; the daily mean and standard deviation of the error values for the Beer's-type and raytrace models were $13\% \pm 10\%$ and $8\% \pm 6\%$, respectively. The results confirm previously known limitations of Beer's Law when used to estimate sub-canopy solar beam irradiance under heterogeneous canopy conditions. Averaged over the spatial domain, the Beer's-type model estimated 21% and 48% lower canopy transmittance than the raytrace model on 01 March and 03 May, respectively. The Beer's-type model was unable to represent the seasonal increase in areal average canopy transmission contributed from small canopy gaps. Finally, both distributed models were used to simulate the cumulative solar beam irradiance during the 2010 snowmelt season. The raytrace model was shown to capture a high level of variability necessary to simulate explicit stand-scale solar irradiance that strongly influences spatiotemporal patterns of snowmelt, soil water availability, and the partition and exchange of energy within heterogeneous forest ecosystems.

© 2013 Elsevier Inc. All rights reserved.

1. Introduction

The magnitude of solar radiation incident on a forest floor is a major component of the sub-canopy surface energy budget and plays an important role in diurnal latent and sensible heat fluxes in forested areas. It has broad implications on fuel moisture and wildfire hazard (e.g., Byram & Jemison, 1943) and seasonal snow water availability (e.g., Golding & Swanson, 1978). Incoming shortwave radiation (i.e., 250–2500 nm wavelength band) is also a primary forcing variable required by land surface and hydrological models to estimate soil temperature and water content and snowpack temperature and water equivalent.

Compared to above-canopy global shortwave fluxes, the radiation at the forest floor exhibits enhanced spatial and temporal variability as a result of the sky track of the sun and the relative orientation of terrain, canopy elements, gaps and clearings (e.g., Essery et al., 2008; Gay et al., 1971; Pomeroy et al., 2008; Reifsnyder et al., 1971). Conversely, diffuse solar radiation shows remarkable uniformity even under heterogeneous canopy conditions (e.g. Pomeroy et al., 2008; Reifsnyder et al., 1971). The variability of the sub-canopy solar beam makes it impractical to use ground-based measurements to estimate seasonal dynamics of the diurnal mean and variance of surface irradiance over spatial domains (e.g., 900 m² to 1 km²). These scales are of particular interest given that remotely sensed canopy metrics (e.g., leaf area index or forest cover fraction) are derived at these intermediate scales.

In land surface and hydrological models, canopy transmittance is commonly estimated using effective leaf area index (i.e., *LAI'*) within a variant of the Beer–Lambert law (Monsi & Saeki, 1953), hereafter

* Corresponding author at: Centre for Hydrology, University of Saskatchewan, 117 Science Place, Saskatoon, Saskatchewan, S7N 5C8, Canada. Tel.: +1 403 688 4881.

E-mail address: keith.musselman@usask.ca (K.N. Musselman).

referred to as a Beer's-type transmittance model. The method assumes an exponential reduction of solar radiation through a random distribution of elements (Campbell & Norman, 1989). Various schemes have been introduced to simulate the effect of canopy gaps and clumping (i.e., non-randomness) (e.g., Chen et al., 1997a; Ellis & Pomeroy, 2007; Nijssen & Lettenmaier, 1999). The resulting mathematical approximations are generally adequate to estimate the average daily sub-canopy irradiance, although uncertainty increases with canopy heterogeneity (Pinty et al., 2004). Notwithstanding, the Beer's-type approach may have limited utility for simulating nonlinear processes such as those governing snowmelt (Gray & Male, 1981) when the assumption of a homogeneous canopy is not satisfied (e.g., canopy edges around forest gaps and clearings). To address this issue, a recent study used high-temporal resolution estimates of solar direct beam canopy transmittance from upward looking hemispherical photographs to improve sub-canopy snowmelt model accuracy (Musselman et al., 2012a). The results highlighted the utility of detailed canopy information as well as the nonlinear melt behavior of snow cover. Hemispherical photo estimates of solar direct beam canopy transmittance can be advantageous compared to expensive ground-based sensor options that require regular maintenance, particularly in seasonally snow-covered environments. Like ground-based sensors, however, the canopy information from photos is limited to specific locations and does not provide information about the spatial patterns of canopy transmittance.

Models capable of simulating spatially explicit, physically based processes can improve the integration between traditional monitoring and modeling techniques. Advances at these scales will ultimately improve understanding and prediction of hydrological states and fluxes and associated feedbacks with climate and ecological processes at larger scales (Bales et al., 2006). In this regard, high-resolution models can be used to evaluate scale discontinuities between ground-based observations and larger-scale processes commonly measured by remote sensing techniques or simulated by land surface or climate models. For example, high-resolution spatially distributed canopy transmittance estimates could be used to force snow models at the stand-scale for evaluation against ground-based measurements and remotely sensed snow covered area products (e.g., Raleigh et al., 2013; Varhola et al., 2012). This type of analysis is critical in steep, forested terrain where few ground-based measurements exist, seasonal snow cover duration is prolonged, and the accuracy of remote sensing products is unresolved (Molotch & Margulis, 2008).

Airborne scanning light detection and ranging (LiDAR) has increasingly been used to estimate biophysical canopy parameters such as canopy cover and: LAI' (e.g., Korhonen et al., 2011; Lefsky et al., 1999; Lovell et al., 2003; Morsdorf et al., 2006) as well as forest stand biomass (e.g., Frazer et al., 2011) and canopy light transmittance (e.g., Essery et al., 2008; Parker et al., 2001; Todd et al., 2003; Varhola et al., 2012). Frazer et al. (2011) provides a general description of how spatially explicit forest parameters are commonly obtained from LiDAR and ground-based measurements. For example, analogs exist between the physics used in canopy measurements from LiDAR and the indirect estimation of canopy metrics from upward looking hemispherical photography using gap fraction techniques. Particularly, photo-derived LAI' has been shown to be closely and inversely proportional to LiDAR-derived canopy penetration indices computed at photo locations (Corona et al., 2012; Morsdorf et al., 2006). The Laser Penetration Index (LPI) (Barilotti et al., 2006) is defined as the fraction of all point returns classified as ground normalized by the total return count:

$$LPI_{ij} = \frac{mG_{ij}}{mG_{ij} + mV_{ij}} \quad (1)$$

where mG_{ij} and mV_{ij} are the number of ground and vegetation returns per unit area, respectively. Subscripts i and j refer to the respective grid cell column and row. The normalization of ground returns by total returns removes local variations in the sampling density as a result

of overlapping flight paths. Improved relationships between LPI and photo-based LAI' are obtained when LiDAR returns are averaged over a spatial domain centered on each grid element (e.g. Morsdorf et al., 2006). The spatial averaging of the ground and vegetation returns is analogous to how LAI' is determined from a hemispherical photo (i.e. computed over many zenith and azimuth ranges (Campbell & Norman, 1989)). The spatial extent of LiDAR data averaging necessary to obtain the best agreement with photo-derived LAI' varies as a result of view geometry differences between the photos and LiDAR, local vegetation density, and canopy height (Morsdorf et al., 2006). For example, Barilotti et al. (2006) reported an improved relationship between ground-based LAI and LiDAR-derived LPI when the ground and vegetation returns were smoothed using a 5 m nearest-neighbor filter. Morsdorf et al. (2006) conducted a sensitivity analysis and found the best agreement with 15 m circular averaging. The results indicate that ground calibration is an important step to generating an LAI' proxy from LiDAR returns.

The field-calibrated spatial map of LAI' could be used within a Beer's-type model to simulate spatially explicit canopy transmittance at high-resolution. The results, however, would face similar limitations to those of point-scale radiative transfer applications of a Beer's-type approach in heterogeneous forest environments (e.g., Pinty et al., 2004) in that the method is not directionally explicit with regard to the sun's position relative to canopy gaps.

A treatment of directionality of solar canopy transmittance is possible using ray tracing methods to evaluate the impact of the 3-D canopy orientation on the solar beam transmittance. For example, a 3-D raytrace model populated with LiDAR-derived forest structure promises to yield the most physically realistic estimates of solar canopy transmittance in heterogeneous forested terrain. To date, no studies have explicitly simulated the sub-canopy solar beam canopy transmittance at high spatial (i.e., 1-m) and temporal (i.e., 5-min) resolution for a stand-scale (i.e., $>0.5 \text{ km}^2$) topographically complex forested area.

The objective of this paper is to evaluate the use of airborne LiDAR data to estimate solar direct beam canopy transmittance. Photo-derived, high-resolution estimates of solar beam canopy transmittance were used to evaluate two spatially distributed canopy transmittance models: 1) a Beer's-type transmittance model based on LiDAR-derived LAI' and forest cover fraction, and 2) a solar raytrace model applied to a 3-D canopy derived from multiple LiDAR flights. Finally, the two models were used to estimate the cumulative solar beam irradiance for the 2010 snowmelt season in the southern Sierra Nevada. The paper is organized as follows. Section 2 presents the data acquisition, study area, and a description of the hemispherical canopy photographs and airborne scanning LiDAR data processing. Sections 3 and 4 detail methods used to estimate spatially explicit solar direct beam canopy transmittance from LiDAR including a Beer's-type approach (Section 3) and a raytrace model (Section 4). Evaluation methods are presented in Section 5. Section 6 includes the results and discussion and Section 7 highlights the conclusions.

2. Data collection and processing

2.1. Study site

Work was conducted within the Wolverton basin of Sequoia National Park, California, USA (36.59°N, 118.717°W) (Fig. 1). The forest in the region is predominantly mature red fir (*Abies magnifica*). The average LiDAR-derived tree height was $32 \text{ m} \pm 9 \text{ m}$ (the tallest trees exceeded 60 m heights) and the canopy was largely discontinuous in nature with many gaps and a few larger meadows (Fig. 1). A 7 m domain-average canopy diameter was determined by manual analysis of canopy pixels (Fig. 1) for individual trees within two $100 \text{ m} \times 100 \text{ m}$ sub-domains.

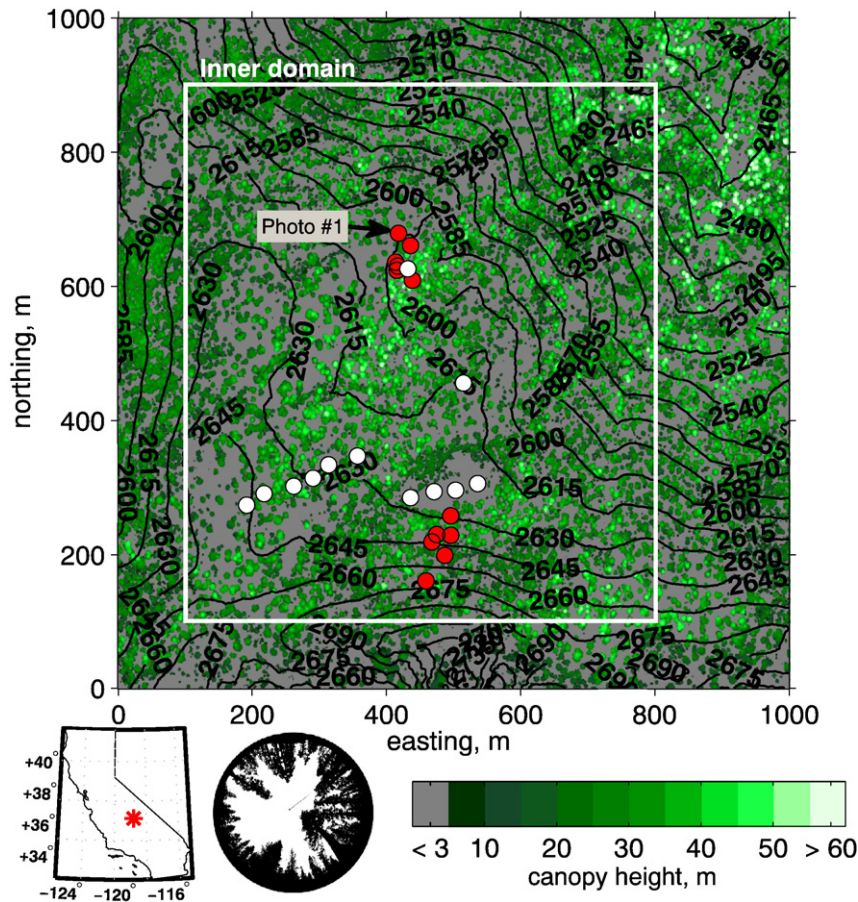


Fig. 1. The study area and inner model domain showing the elevation contours in 15 m increments, the LiDAR-derived canopy height, and the locations of hemispherical photographs used for calibration of the ray-tracing model (empty circles) and analysis (filled circles). The location and image of Photo #1 are included.

Data analyses were conducted within two spatial domains, an outer and an inner domain (Fig. 1). The outer domain was 1 km \times 1 km and ranged in elevation from 2420 m to 2757 m. The 800 m \times 700 m inner sub-domain (Fig. 1) was used to estimate direct beam canopy transmittance as described in Sections 3 and 4. The domain extent and nesting was chosen to include a high local ridgeline to the south and a smaller north–south oriented ridge to the west; the configuration ensured that any local terrain that might cast shade on the inner domain was included within the outer domain boundary.

2.2. Hemispherical canopy photographs

Twenty-four upward-looking canopy photographs were obtained within the model domain at locations indicated in Fig. 1. Photos were taken in September 2009 under low light conditions for improved contrast between vegetation and sky. The camera was mounted at a height of 1.5 m, leveled and oriented as in Frazer et al. (2000). The photo processing software Gap Light Analyzer (GLA) Version 2.0 (Frazer et al., 1999) was used to georegister and classify images as sky and non-sky elements (see example in Fig. 1). The binary pixels were aggregated into discrete sky regions to determine the directional sky view factor at one-degree angular resolution as in Musselman et al. (2012b).

The photos were used to estimate explicit, time-variant direct beam canopy transmittance at five-minute temporal resolution for each of the 24 photo locations for all days between the winter and summer solstices (see Musselman et al., 2012b). Solar beam transmittance was estimated by sampling the fraction of sky to total pixels within a one-degree pixel corresponding to the solar coordinates. Explicit transmittance estimates from 12 of the 24 photos (calibration photos; Fig. 1) were used to calibrate the raytrace model (see Section 4).

The remaining 12 photos (analysis photos; Fig. 1) were used to evaluate two LiDAR-derived, spatially distributed canopy transmittance models: (1) a Beer's-type model (see Section 3) and (2) a ray tracing model (see Section 4). The 12 analysis photos were chosen to correspond to locations of automated snow depth sensors described in Musselman et al. (2012a, 2012b).

2.3. Airborne scanning LiDAR data

The National Center for Airborne Laser Mapping (NCALM) obtained LiDAR data during flights flown over the region in March (i.e. snow-on) and August (i.e. snow-off) 2010. Data were obtained with an Optech (Toronto, Canada) Gemini Airborne Terrain Mapper (ALTM) mounted in a twin-engine Cessna Skymaster. The ALTM emits a pulse rate of 167 kHz at a wavelength of 1064 nm and includes up to four range measurements; first, second, third, and last returns with a scan angle range of $\pm 14^\circ$ (NCALM, 2012). The return classification information was provided within the LAS binary file format (ASPRS, 2012) produced by NCALM. The point data classified as surface returns were used by NCALM to produce Digital Terrain Models (DTM) at 1 m spatial resolution from the August flight data (i.e. ground height; DTM_{ground}) and the March flight data (i.e. snow surface height; DTM_{snow}) using a filter method similar to that of Kraus and Pfeifer (1998) (NCALM, 2012). These gridded products were used to separate surface returns from forest canopy returns as described in Section 3. The March and August flights yielded all-return mean point density values within the domain of 11.5 returns m^{-2} and 14.6 returns m^{-2} , respectively. To evaluate the best agreement between LPI and photo-derived LAI , three point cloud data products were analyzed: March flight returns, August flight returns,

and a combined product of all returns from both flights (see Section 3). The combined flight data were examined for their potential to represent an increased sample density of the 3-D canopy space. Using the combined returns from both flights, the forest structure (i.e. excluding surface returns) was represented with a domain-average canopy return density of 18.259 returns m^{-2} ; a total of 18.259 million returns over the 1- km^2 domain.

3. Beer's-type model of solar direct beam canopy transmittance from LiDAR

The Beer's-type model used to estimate canopy transmission is presented in Appendix A. The model is based on estimates of LAI' from hemispherical photos (e.g., Black et al., 1991; Campbell & Norman, 1989). The model is modified specifically for the direct beam as in Gryning et al. (2001) by reducing transmittance through canopy gaps with a geometric shading factor that accounts for the effect of tree geometry and solar elevation angles on gap transmission. The Gryning et al. (2001) modification represents one of the more physically realistic Beer's-type approaches for estimating shortwave canopy transmittance in sparse forests. The extension of the Beer's-type model to a spatial domain, however, requires distributed estimates of canopy openness and LAI' .

Ground-based LAI' estimates were obtained from the twenty-four hemispherical photos as described in Appendix B. The 24 LAI' measurements were used to derive a spatial LAI' proxy from the LiDAR-derived

LPI (Eq. (1)). A threshold value of 1 m above the DTM_{snow} height was chosen to separate ground/surface returns from forest canopy returns. Values above this threshold were considered canopy returns and included in mV_{ij} in Eq. (1). Values below this threshold were considered surface returns (mG_{ij} in Eq. (1)). The threshold provided a buffer to ensure the accurate classification of forest canopy returns and to provide a fair evaluation of ground-based LAI' and LPI computed from returns from the snow-on March flight, the snow-off August flight and the combined returns from both flights (Fig. 2).

The three LPI products were evaluated against ground-based LAI' values to determine the optimal LAI' proxy used in the Beer's-type model. A sensitivity test was conducted to evaluate the effect of circular averaging on the statistical relationship between LAI' and LPI at photo locations as in Morsdorf et al. (2006). Filter radii of 5 m to 100 m in five-meter increments were used to produce 20 LPI maps (i.e. LPI_{circ}) in addition to the native 1 m LPI map. The sensitivity test was conducted separately for LPI values computed from the March, August, and combined flight returns (a total of 60 LPI maps). The LPI_{circ} values corresponding to the 24 photo locations (Fig. 1) were sampled from each product. The (linear) regression computed on photo-derived LAI' and LiDAR-derived LPI_{circ} that resulted in the highest R^2 and lowest p-value was used to determine the optimal LiDAR flight dataset and circular filter radius used to develop the LAI' proxy over the inner model domain at 1 m horizontal resolution.

The LiDAR-derived forest cover fraction f_c (Eqs. (A4)–(A6)) needed for the Beer's-type model was specified as: $f_c = 1 - LPI_{circ-opt}$, where

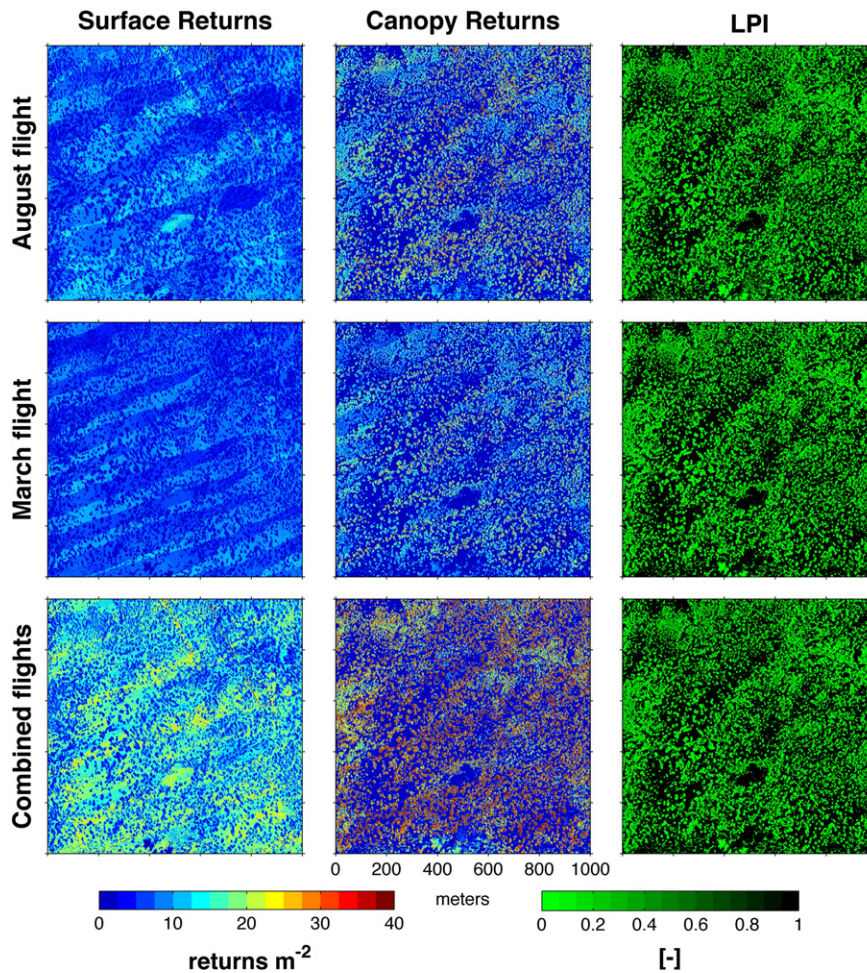


Fig. 2. The number of LiDAR surface returns (i.e. mG ; left column) and canopy returns (i.e. mV ; center column) per square meter used to estimate the Laser Penetration Index (i.e. LPI ; right column) at one-meter horizontal grid spacing. The data from the August (top row), March (middle row), and the combined flights (bottom row) are shown.

$LPI_{circ-opt}$ was the optimal value determined from the circular filter sensitivity test described above. The distributed forest cover fraction and LAI' products were then used in a Beer's-type estimation of solar direct beam canopy transmittance following methods detailed in Gryning et al. (2001) and summarized in Appendix A.

4. Raytrace model of solar direct beam canopy transmittance

A generalized flow chart of the main components of the raytrace model is provided in Fig. 3. The model consists for two main components: the 3-D voxel canopy model and the raytrace model.

4.1. Voxel-based canopy structure model

The 1-km² 2-D domain was given a 340 m vertical dimension defined by the elevation difference between the highest terrain or vegetation height in the domain and the lowest terrain elevation. The 3-D domain was discretized into cubic volumes called voxels. An edge length of 1 m was specified for each voxel; a total of 1000 × 1000 × 340 elements or 340 million voxels. The element size was chosen to ensure both an adequate point return density per element and to make the dataset computationally efficient. For example, smaller volumetric elements would decrease the per element

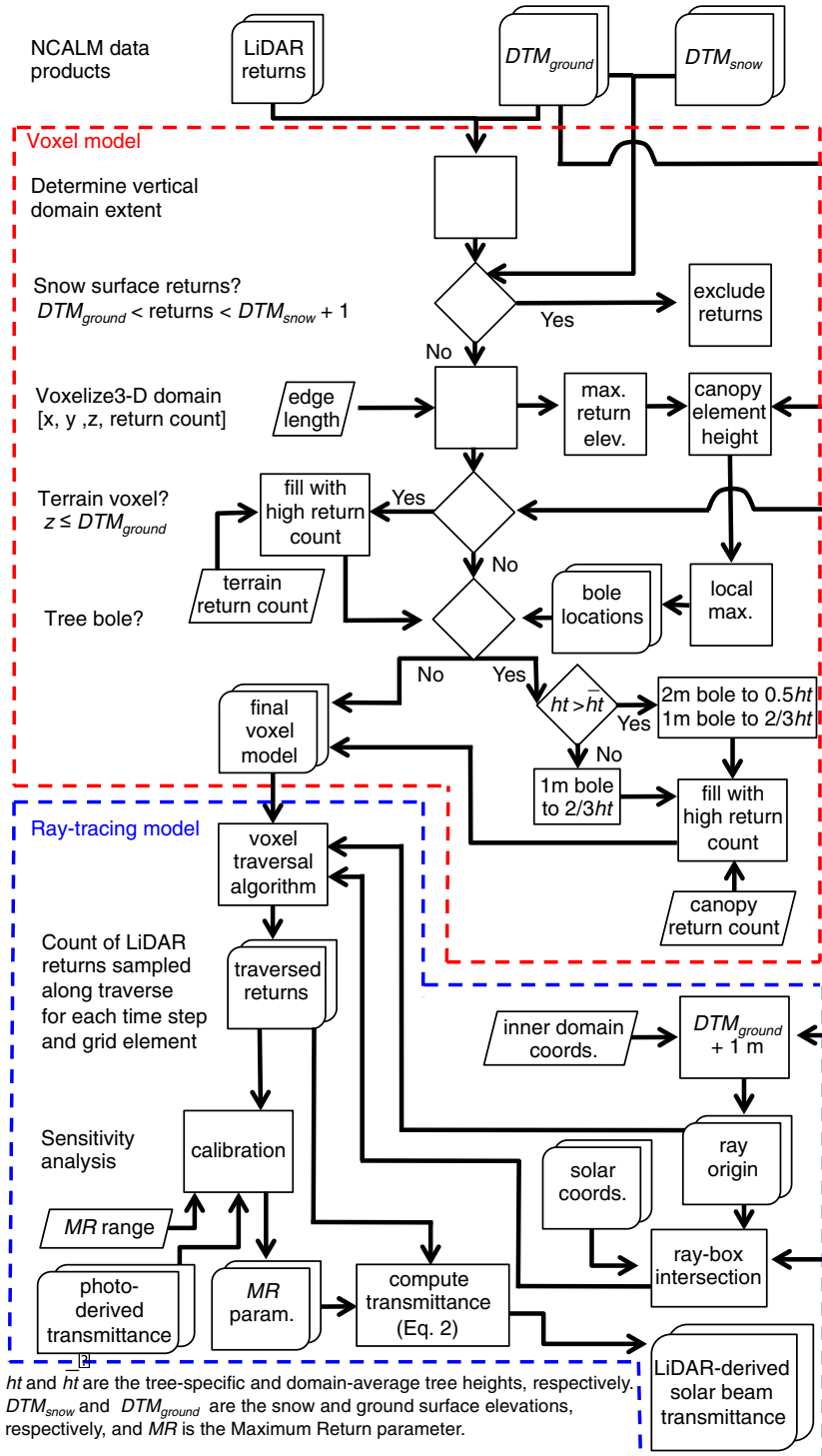


Fig. 3. Generalized flow chart of the voxel and raytrace model procedures used to estimate solar direct beam canopy transmittance from LiDAR data.

point return density (i.e., the canopy model robustness) and increase the likelihood that elements would be unsampled by the LiDAR system (e.g., Hagstrom & Messinger, 2012). In this study, the large scale of the trees ensured that the one-meter voxel edge length adequately captured the general forest architecture. Note that the edge length was approximately 3% and 14% of the domain-average tree height and canopy diameter, respectively. Additionally, the LiDAR horizontal error in terrain with large topographic relief has been reported to be as high as 1 to 2 m (Cho et al., 2011). While the point cloud georegistration errors were not evaluated in this study, the 1 m voxel size was deemed adequate to minimize misrepresentation of the general forest structure resulting from horizontal uncertainty.

The canopy returns were binned in the voxel space according to the 3-D return coordinates. The March flight data classified as (snow) surface returns were excluded from the voxel model by excluding return heights that met the condition: $DTM_{ground} < \text{return elevation} < DTM_{snow} + 1$ (Fig. 3). The exclusion of near-surface returns ensured that the LiDAR point data only contained information from forest vegetation as it might impact the viewshed of a tripod-mounted hemispherical photo or radiation at the snow surface; note that the seasonal maximum snow depth within the domain was approximately 3 m in 2010 (Musselman et al., 2012b) and understory vegetation was generally lower than the 1.5 m height of a hemispherical photo. Each voxel was prescribed a value corresponding to the number of point returns contained within that voxel extent. Voxels within which no returns were measured were prescribed a value of zero. Terrain was represented by filling the voxel space from the lowest domain layer to the DTM_{ground} elevation as in Pyysalo et al. (2009). Voxels representing terrain were specified to contain an arbitrarily high return count of 50.

Because airborne LiDAR measures the forest canopy from above, occlusion by higher canopy elements reduces the probability that lower branches and tree boles will be sampled (Popescu & Zhao, 2008). In general, field observations of the red fir trees indicated reduced branch structure in the lower half of the tree, but the tree bole volumes were significant and must be accounted for in a 3-D raytrace model. The horizontal position of an individual tree bole can be estimated to be approximately beneath the tallest part of an individual tree top (Popescu & Zhao, 2008). A simple local maxima algorithm was applied to the voxel height data that identified pixels in which the canopy height exceeded that of the eight nearest neighbors. Tree boles were represented in the voxel model at the location of the local maxima by filling the voxel space from the DTM surface to a height of two-thirds the total tree height. The two-thirds value was arbitrarily chosen to represent the tapering diameter of the average tree bole with height (Gray, 1956) and to ensure that the modeled bole extended into the crown. The upper portion of a tree canopy is much more likely to be sampled by the airborne LiDAR (Popescu & Zhao, 2008) thus negating the need to fill the voxel space and the potential for over-representing the bole diameter in the upper canopy. The bole diameter of the larger trees in the domain exceeded the 1 m voxel edge length and in some cases exceeded three meters. For this reason, the 32 m average tree height was used to partition trees into 1 m and 2 m bole diameters. Trees of height ≤ 32 m were specified a 1 m diameter bole as previously described. Trees of height > 32 m were specified a 2 m diameter tree bole extending to a height of one-half the tree height and a 1 m diameter bole further extending to a height of two-thirds the tree height. The boles were represented within the structured voxel grid by a stack of single voxels in the case of a 1 m bole and a 2×2 horizontal group of vertically stacked voxels in the case of a 2 m bole. Voxels representing tree boles were specified an arbitrarily high return count of 50 as done with terrain.

4.2. Raytrace model

A simple voxel traversal algorithm (Amanatides & Woo, 1987) was performed on each surface grid element within the inner model

domain (Fig. 3). The slope and direction of each ray were defined by the solar elevation and azimuth angles, respectively, for a given time step. The solar coordinates were computed as in Reda and Andreas (2004) at five-minute time steps for daylight hours (i.e., solar elevation $> 0^\circ$) for every seven days between 21 December and 22 June. The seven-day interval was chosen to reduce computational demand while still capturing the seasonal variability in the sun's sky track.

The first component of the raytrace model required the initialization of the ray origin within the $[800 \text{ m} \times 700 \text{ m} \times 340 \text{ m}]$ inner domain (Fig. 3). For convenience, rays were initiated near the terrain surface of each grid element and traversed the voxel space in the direction of the sun. The ray origins were defined as 1 m above the inner-domain LiDAR-derived DTM_{ground} height. Also required were the 3-D coordinates of the intersection between each ray and a bounding box defined by the $[1000 \text{ m} \times 1000 \text{ m} \times 340 \text{ m}]$ outer domain. The 3-D intersection coordinates were computed for each surface grid element and time step of interest. The second component of the voxel traversal algorithm was the calculation of the incremental traverse of the voxel space along a 3-D line defined by two points: the origin and the intersection with the outer domain boundary (Fig. 3). A computationally efficient digital 3D line drawing algorithm (Amanatides & Woo, 1987) was used to identify which voxels to sample along a given ray path. For each time step and grid element, the total count of canopy returns that were encountered along the ray traverse was recorded. For example, if a ray originated at a grid element located in a clearing at solar noon and only traversed empty voxels (i.e., elements that did not include point returns) a value of zero was recorded for that grid element and time step. Conversely, if a ray bisected dense canopy at a low solar elevation angle, the total returns accumulated along the voxel traverse was high. The end result was a data array $[800 \text{ m} \times 700 \text{ m} \times (\text{five-min. daylight time steps}) \times (27 \text{ seven-day intervals between and including the solstices})]$ containing total return counts for each raytrace.

4.3. Raytrace estimate of solar direct beam canopy transmittance

It is assumed that solar direct beam canopy transmittance is similar to that of a laser beam passing through the canopy (Barilotti et al., 2006). In this regard, physical similarities likely exist between the solar beam passing through the forest and the accumulated LiDAR point returns along a ray-voxel traverse. A maximum return (MR) parameter is presented that represents an upper limit of accumulated point returns along a given ray path, above which threshold value full canopy attenuation of the incoming solar direct beam is assumed. Time series of direct beam canopy transmittance $DBT_{ij}(t)$ at each photo location (i,j) were computed as

$$DBT_{ij}(t) = 1 - \frac{\text{MIN}(\text{returns}_{ij}(t), MR)}{MR} \quad (2)$$

where $\text{returns}_{ij}(t)$ represents the accumulated LiDAR point returns along a ray path originating at the photo location at time step t . A sensitivity test was conducted to evaluate the MR parameter and the relationship between the explicit photo-derived direct beam canopy transmittance and the raytrace model results. A subset of 12 of the 24 photographs was used to calibrate the MR parameter. The mean absolute error (MAE) was computed between the explicit photo-derived direct beam canopy transmittance and that derived from the raytrace model for MR parameter values ranging from 1 to 300. The MR value that minimized the average MAE from all 12 photos was used to compute the raytrace-derived solar direct beam canopy transmittance (Eq. (2)) for the inner model domain and all time steps. The remaining 12 photos were reserved for independent verification analysis and comparison of results to the Beer's-type canopy transmittance model as described in the next section.

Finally, a linear interpolation was applied to the 5-min canopy transmittance values simulated at seven-day intervals to estimate the solar direct beam canopy transmittance at 5-min time steps for all days between the winter and summer solstices.

5. Evaluation methods

The bulk and raytrace estimates of solar direct beam canopy transmittance were first evaluated against the explicit photo-derived canopy transmittance product of Musselman et al. (2012b) at locations of 12 hemispherical photos (i.e., the point-scale). The result from these 12 locations was a time series of canopy transmittance error values for every five-minutes of each simulated day. Two metrics were evaluated: 1) the normalized daily error and 2) the normalized daily absolute error. The normalization of the canopy transmittance errors involved a temporal weighting based on the above-canopy simulated clear-sky incoming solar radiation magnitude. Clear-sky global incoming solar radiation at five-min. time steps (i.e. $R_{S\downarrow clear,t}$) was computed as in Allen et al. (2006). The weighting scheme was first applied to obtain daily mean error values, \bar{x}_i ,

$$\bar{x}_i = \frac{\sum_{t=1}^n R_{S\downarrow clear,t}}{\sum_{t=1}^n R_{S\downarrow clear,t}} x_t \quad (3)$$

where x_t is the transmittance error at five-min. diurnal time steps t when the sun is above the horizon. For example, canopy transmittance errors that occurred early in the day under low potential solar magnitude were weighted less than transmittance errors that occurred at solar noon. A second weighting scheme was applied to \bar{x}_i for all simulated days i to compute the seasonal weighted daily mean canopy transmittance, \bar{x}_s as

$$\bar{x}_s = \frac{\sum_{i=1}^n R_{S\downarrow maxclear,i} \bar{x}_i}{\sum_{i=1}^n R_{S\downarrow CJ}} \quad (4)$$

where $R_{S\downarrow maxclear,i}$ is the maximum daily clear-sky solar radiation and $R_{S\downarrow CJ}$ is the annual maximum clear-sky solar radiation (i.e. on 21 June). For example, daily mean canopy transmittance errors occurring on the date of the winter solstice were thus weighted less than daily mean errors occurring late in the spring under conditions of high incoming solar irradiance.

Additionally, the Beer's-type and raytrace estimates of direct beam canopy transmittance were compared for sample days of 01 March and 03 May. The two dates, separated by two months, were chosen as illustrative examples of the variability in solar canopy transmittance patterns for late winter and early spring conditions. Finally, the two distributed canopy transmittance models were used to estimate the cumulative solar beam irradiance over the domain for the 2010 snowmelt season. Above-canopy hourly measurements of global incoming solar radiation were linearly resampled to five-min values and empirically disaggregated into the direct and diffuse components as in Allen et al. (2006). The radiation measurements and disaggregation are presented in Musselman et al. (2012a, 2012b). The cumulative direct beam solar irradiance was computed by multiplying the above-canopy direct beam radiation by the transmittance for the corresponding five-minute time step. The cumulative sum was calculated

in units of $MJ\ m^{-2}$ for the period of 01 March to 21 June 2010, corresponding to the spring snowmelt period.

6. Results and discussion

6.1. LiDAR-derived LPI and LAI'

The combined returns from both LiDAR flights produced the highest R^2 value of 0.64 (Table 1) when linear regressions between photo-derived LAI' and LPI_{circ} produced with varying circular filter radii were evaluated (Fig. 4a). The improved relationship indicates that the combined point cloud produced the best agreement with ground-based LAI' and therefore may provide a better canopy representation than a single flight. The combined canopy returns from both flights were used in the remaining analysis. The implications and potential uncertainty resulting from the use of a multi-flight point cloud are discussed in Section 6.6.

Poor statistical results between photo-derived LAI' and LPI_{circ} were obtained when LPI_{circ} was computed with very short (e.g. 10 m) and long (e.g. 60 m) radial lengths. Examples of three linear regressions between the two metrics are shown for filter radii of 10 m, 35 m, and 60 m (Fig. 4b–d). Illustrative examples of the LPI maps produced with these filter radii are provided in Fig. 4e–g. The short lengths resulted in highly variable LPI values; effectively sampling only the part of the canopy that would appear at low zenith angles (i.e., directly overhead) in a hemispherical photo. Conversely, long filter radii resulted in lower LPI variability by averaging more of the canopy than would be viewable from a hemispherical photo as a result of canopy occlusion. The 35 m radius filter produced the highest R^2 value (0.64) and lowest p-value ($p = 0.01$) (Fig. 4) and the resulting regression was chosen to create an LAI' proxy from LPI using the combined return product as

$$LAI' = -5.059 LPI_{35m_y} + 4.57 \quad (5)$$

The resulting LAI'_{ij} from Eq. (5) is provided in Fig. 5. The LPI_{35m} metric (Fig. 4f) was also used to specify the forest cover fraction for each grid element (i.e., $f_{c_{ij}} = 1 - LPI_{35m_{ij}}$). The statistical relationship was developed from LAI' measurements made at 24 locations spanning a range of canopy conditions representative of the domain (see Fig. 1). It is likely that Eq. (5) would not apply to other regions or forest stands. In addition, the equation predicted negative LAI' values when $LPI_{35m} > 0.903$, which only occurred in the center of the largest meadow. In these instances, LAI' was constrained to zero.

6.2. Raytrace estimate of solar direct beam canopy transmittance

On average, an MR parameter value of 42 produced a minimum mean absolute difference value of 0.14; the average mean absolute difference increased both below and above this value (Fig. 6). The optimal MR parameter indicates that if a ray traverses a linear voxel space and encounters at least one and fewer than 42 canopy returns, a fraction of the direct beam will be transmitted and the remaining fraction will be attenuated (reflection is not considered). If no returns were accumulated along the ray traverse, the direct beam is assumed

Table 1

The LiDAR flight metrics and results of the sensitivity analysis of LPI averaged with circular filter radii that obtain the best fit with photo-derived LAI'. The combined returns from both flights produced the best agreement with ground-based data and were chosen for analysis.

| Flight | Total returns (million) | Mean surface returns m^{-2} | Mean vegetation returns m^{-2} | Mean LPI | Filter radius (m) producing best fit to photo LAI' | R^2 at optimal filter radius |
|----------|-------------------------|-------------------------------|----------------------------------|------------------|--|--------------------------------|
| March | 11.52 | 5.7 | 5.8 | 0.628 ± 0.40 | 35 | 0.619 |
| August | 14.65 | 7.9 | 6.7 | 0.606 ± 0.39 | 35 | 0.615 |
| Combined | 26.16 | 12.8 | 13.4 | 0.634 ± 0.39 | 35 | 0.639 |

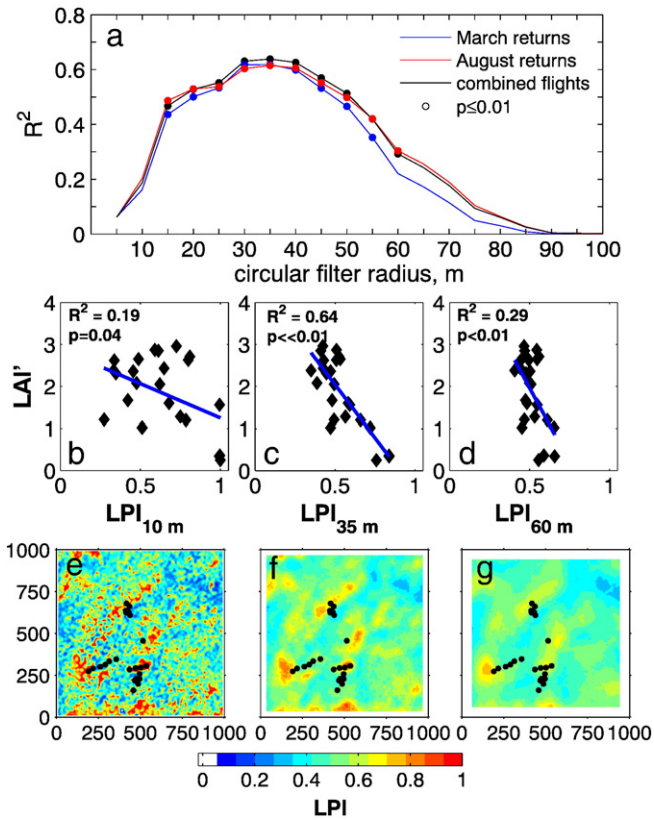


Fig. 4. (a) The coefficient of determination (R^2) of the linear regression between photo-derived LAI' and the LiDAR-derived laser penetration index (LPI ; one-meter native resolution) computed with a circular filter centered on the photo location with filter radii of 5 m to 100 m in five meter increments computed from the March, August, and combined flight datasets. The markers represent linear regressions with p -values ≤ 0.01 . Examples of the linear regressions between LAI' (y-axes) and LPI (x-axes) for LPI computed with filter radii of (b) 10 m, (c) 35 m, and (d) 60 m computed on data from the combined flights. The LPI maps created with the (e) 10 m, (f) 35 m, and (g) 60 m filter radii are included beneath the corresponding linear regression plots. The 24 photo locations used in the regression analysis are indicated.

to pass unimpeded. Conversely, 42 or more accumulated returns correspond to full canopy attenuation of the solar direct beam.

6.3. Point-scale comparison of the raytrace and Beer's-type models

The explicit, photo-derived product (Fig. 7a) illustrates the way in which distinct canopy elements can impact the solar beam transmittance at a given time and how the transmittance changes with

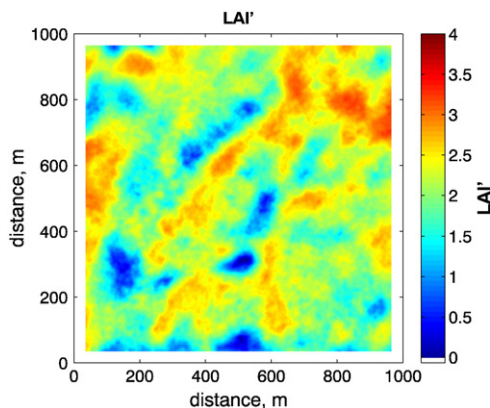


Fig. 5. LAI' determined from linear regression between 24 hemispherical photographs and LiDAR-derived LPI at one meter horizontal grid spacing averaged with a 35 m radius circular filter centered on each grid element.

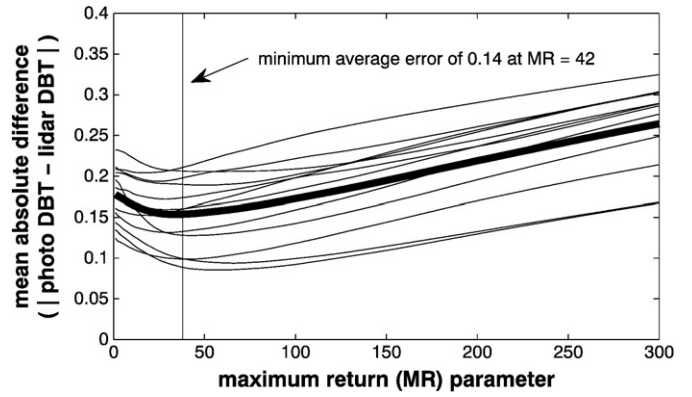


Fig. 6. The mean absolute difference (y-axis) between solar direct beam canopy transmittance (DBT) derived from hemispherical photos and LiDAR at 12 locations for a range of maximum return (MR) values (x-axis). The bold line indicates the average values from the 12 locations. The vertical line indicates the MR value that minimized the mean absolute difference between the photo- and LiDAR-derived DBT products when averaged at 12 locations.

seasonal sun angles. The raytrace results in Fig. 7b show a marked similarity to the explicit photo results. Conversely, the example of the Beer's-type model (Fig. 7c) highlights the limited information available when canopy structure is inherently directionally invariant.

Both the photo and LiDAR transmittance products at the location of Photo #1 indicate a large canopy gap in the south and east that results in a prolonged period of high transmittance, particularly in the morning and after 01 April (Fig. 7; note that east is to image left, consistent with upward hemispherical view geometry when oriented with north at the image top). The two products also show a cluster of trees to the south and west that limits beam transmittance after noon for much of the year. There were also notable differences between the raytrace and photo estimates. The raytrace estimate exhibits many more fractional transmittance values than the photo estimate. Also, the raytrace estimate underestimates the transmittance signature of the tree cluster to the south and west (afternoon and after ~01 April) (Fig. 7). The greater number of fractional transmittance estimates from the raytrace model is likely a result of the spatial scale discrepancy between the photo and raytrace methods. For example, the high pixel resolution of the photos allows the representation of individual canopy elements (e.g., small branches at close proximity to the photo) that LiDAR is not able to capture with a 1 m voxel edge length. The voxel-based raytrace method implicitly includes the (measured) smaller canopy elements but averages them within a larger volumetric space resulting in the fractional transmittance values.

The left panels of Fig. 8 show quantitatively what is shown graphically in Fig. 7. Both transmittance estimation methods had relatively low but slightly negative normalized daily error at the Photo #1 location from the winter solstice to early February (Fig. 7a–b). After 01 February, the Beer's-type model error increased (i.e. became more negative) with a value below -0.2 from mid-April to mid-May, after which it decreased (i.e. became less negative) to ~ -0.1 by the summer solstice. At the same photo location, the raytrace model exhibited very low normalized error after early February. On average over the year the normalized absolute error was 0.125 for the Beer's-type model and 0.027 for the raytrace model (Fig. 8b).

When averaged at all 12 photo locations, the daily mean normalized error values were again lowest and similar (absolute error values of ~ 0.02) during the winter until early February (Figs. 8c and 7d). The absolute error values of both products were very similar during this time. After early-March the Beer's-type error values became increasingly negative throughout the spring (i.e., underestimated transmittance); from 01 March to 21 June the mean and standard deviation of the daily mean absolute error (across the 12 photo locations) of the Beer's-type and raytrace transmittance estimates

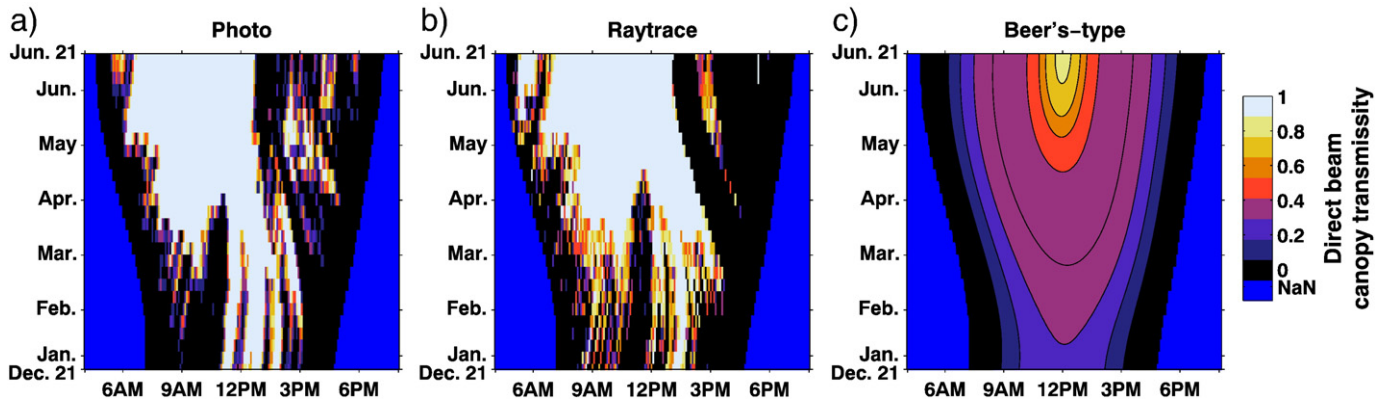


Fig. 7. Solar direct beam canopy transmittance at a single location (photo #1; Fig. 1) determined from: (a) an upward-looking hemispherical photograph, ray tracing of LiDAR-derived 3-D canopy structure (b), and (c) the LiDAR-derived Beer's-type method as shown in the right column of Fig. 6.

were 0.131 ± 0.097 and 0.080 ± 0.055 , respectively (Fig. 8d). The results indicate that the Beer's-type conceptual transmittance model was unable to resolve complex canopy transmission dynamics particularly in late winter and early spring when solar elevations are higher and the sun tracks across a larger sky region. The Beer's-type transmittance errors tended to be strongly biased toward underestimation as inferred from Fig. 8. Conversely, the raytrace model exhibited little to no bias throughout the season.

6.4. Distributed comparison of raytrace and Beer's-type model estimates

The distinct differences in the spatial patterns predicted by the two models (Fig. 9) can be used to inform where and when the Beer's Law approach is acceptable and the conditions under which the underlying assumptions are not met. In general, the raytrace model captured a much higher level of spatial detail and marked differences in magnitude. For example, on 01 March the raytrace model simulated many areas where the direct beam canopy transmittance values exceeded 0.6 while the Beer's-type model limited these higher values to the center of larger forest clearings (yellow, oranges and reds in the left panels of Fig. 9). These model differences are intuitive as the raytrace model provided a more explicit measure of how individual canopy elements impact the direct beam (i.e. directionality) whereas the Beer's-type estimate inherently considers canopy elements in all azimuth directions. Thus, areas that have a clear southern sky view

but dense canopy to the north (e.g., the north side of canopy gaps) will not be well represented by the Beer's-type model. The greatest differences between the raytrace and Beer's-type models for 01 March occurred in and on the north side of canopy gaps (blue color or underestimation by the Beer's-type model) and in areas that receive shading from local terrain (pink color or overestimation by the Beer's-type model) (Fig. 10). It should be noted that the Beer's-type model itself does not account for terrain shading but would generally be computed within a radiation sub-module (e.g., Helbig et al., 2009; Marsh et al., 2012) of a hydrologic model. On average, the model differences on 01 March were 0.039 ± 0.026 , or a 20.7% mean underestimation by the Beer's-type model compared to the raytrace model. This difference was similar in magnitude to the Beer's-type errors computed against photo-derived estimates at the point scale in early March (Fig. 8d). Despite the distinct differences, on 01 March the two models did capture similar large-scale spatial patterns in canopy transmittance resulting from the general orientation of larger forest clearings and areas of denser stands (as inferred from Fig. 1). The similarities indicate that the Beer's-type model tended to perform acceptably in areas where the canopy is homogeneous and lacked directional variation.

The differences between the two model predictions for 01 March were enhanced on 03 May when the sun was higher in the sky and tracked across a greater azimuthal range than in early March. In general, the spatial patterns predicted by the Beer's-type model were similar between 01 March and 03 May and the primary differences were in

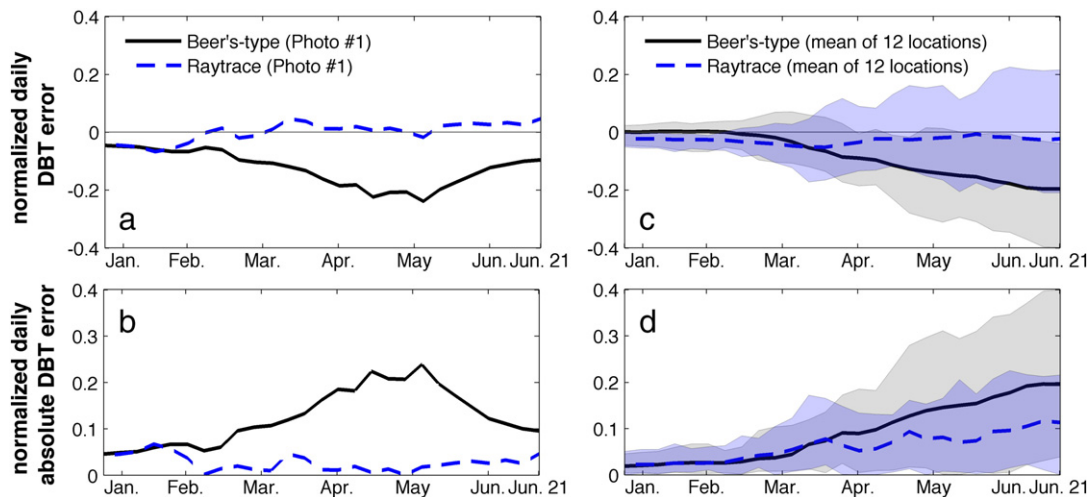


Fig. 8. (a) Daily mean normalized error of solar direct beam canopy transmittance (DBT) estimated from the Beer's-type bulk methods (solid line) and ray tracing (hashed line) evaluated against photo-derived DBT at a single photo location (Photo #1); (b) the absolute value of the normalized DBT error shown in (a); (c) the range (shading) and mean (lines) of the daily mean normalized error determined from the bulk (solid line) and ray tracing LiDAR (dashed line) at 12 photo locations; and (d) the absolute value of the normalized DBT error shown in (c).

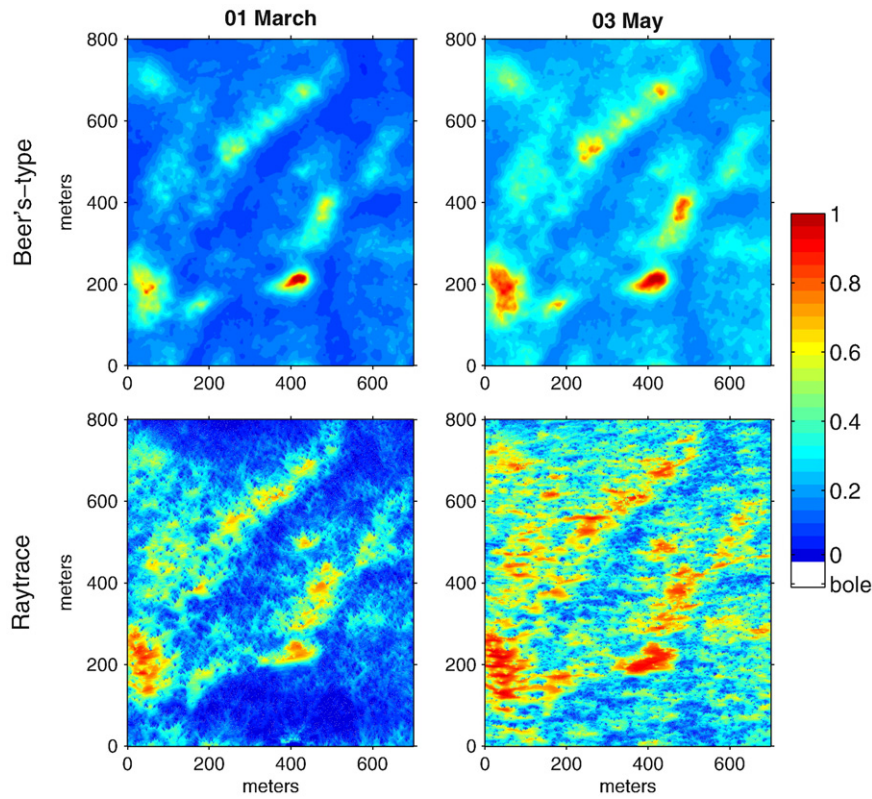


Fig. 9. Modeled normalized daily mean solar direct beam canopy transmittance over the full model domain on 01 March (left panels) and 03 May (right panels) estimated from the Beer's-type (upper panels) and raytrace (lower panels) estimation methods.

the magnitude of the simulated transmittance (Fig. 9, top panels). In contrast, the raytrace model simulated very different spatial patterns and magnitudes of canopy transmittance between March and May (Fig. 9, bottom panels). The spatial patterns of high and low canopy transmittance were elongated along an east–west axis in May compared to March (Fig. 9, bottom-right panel). This is likely a result of the sun rising (setting) in increasingly northeasterly (northwesterly) directions later in the spring. For example, the sun rose above the horizon on 01 March and 03 May at azimuth angles of 99° and 71° , respectively (reported clockwise from north).

The higher late-spring solar elevation and more northerly azimuth angles increased the probability of direct beam canopy transmission in easterly and westerly directions, making the transmittance in these directions more sensitive to canopy structure than in early

March. Late-spring shade cast by individual trees at midday is limited by higher solar elevation angles (69° maximum on 03 May) compared to lower late winter solar elevation angles (46° maximum on 01 March). The higher spring solar elevation angles reduce the sensitivity of canopy transmittance to variations in forest structure to the south. The Beer's-type model was unable to resolve these seasonal variations in solar direct beam canopy transmittance. The average difference between the two models on 03 May was 0.124 ± 0.012 , or a 47.8% underestimation by the Beer's-type model (Fig. 10). Note that this average error value is similar to the 03 May average error value computed between the Beer's-type estimates and the explicit photo results at 12 photo locations (Fig. 8). Qualitative analysis of Figs. 8, 9 and 1 indicates that these underestimates tended to be correlated with areas of high southern sky view (e.g., the north sides of large

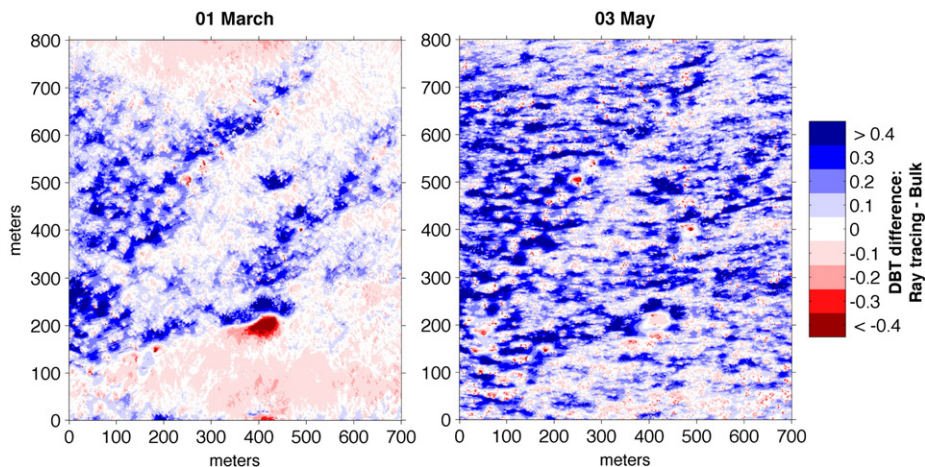


Fig. 10. The difference in normalized solar direct beam canopy transmittance (DBT) estimated with the ray tracing and Beer's-type (i.e. bulk) methods (i.e. 'difference = ray tracing – bulk') for 01 March (left) and 03 May (right).

canopy gaps and meadows) in late winter (i.e., 01 March) and with areas of high sky view slightly south of zenith (e.g., the north side of small canopy gaps) and particularly easterly and westerly sky views in mid-spring (i.e., 03 May).

6.5. Implications for snowmelt modeling

The differences in canopy transmittance predicted by the two models as observed at the point-scale translated to significant differences in both the magnitude and spatial patterns of cumulative direct beam solar irradiance integrated over the 01 March to 21 June 2010 snowmelt period (Fig. 11). Averaged over the 800 m × 700 m domain, the Beer's-type model estimated a mean cumulative irradiance of 428 MJ m⁻² while the raytrace model estimated 631 MJ m⁻²; a 32% average underestimation by the Beer's-type model. Note that the raytrace model is not assumed here to represent the 'truth'. It should also be noted that the Beer's-type model did not uniformly underestimate cumulative irradiance. The scatter plot in Fig. 11 indicates that the lowest irradiance values in the domain were higher for the Beer's-type model than the raytrace model. These model differences generally occurred beneath and in close proximity to individual trees in otherwise open clearings with appreciable sky view. The results highlight the utility of the raytrace model to explicitly simulate the shading influence of individual trees whereas the spatial averaging implicit in the Beer's-type approach lacks this level of detail.

The general patterns of solar beam irradiance integrated over the snowmelt period have implications on the seasonally dynamic spatial patterns of snowmelt and soil water availability. The raytrace model thus provides a level of detail necessary to simulate explicit plot- and stand-scale spring snow cover patterns that can be evaluated against ground measurements. Furthermore, the cumulative irradiance from the solar beam is shown to be important even within the tallest forest stands (60 m heights) where the cumulative irradiance (01 March - 21 June 2010) predicted by the raytrace model commonly reached 600 MJ m⁻² (Fig. 11). This value is the energy equivalent of 167 continuous hours of solar irradiance at 1000 W m⁻², or the snowmelt energy equivalent of 927 mm of melt assuming an average snow albedo of 0.5 and a flat surface; this magnitude of sub-canopy direct beam energy could not be captured by the Beer's-type model.

6.6. Uncertainty and known sources of error

The combination of a winter and summer point cloud would introduce error if snow were present in the canopy at the time of the winter flight. A meteorological station in the center of the model domain recorded daytime maximum temperatures in excess of 7 °C for a five-day consecutive dry period preceding the 22 March flight (Musselman et al., 2012a), indicating a low likelihood of snow in the canopy. The improved relationship with ground-based summer LAI

values obtained with the combined point cloud indicated that the benefit of added canopy structure information from multiple datasets with different flight paths (Fig. 2) may have outweighed potential alignment and georeference discrepancies. The methods presented are equally applicable to data from a single flight.

The photo-derived canopy transmittance estimates were based on the assumption that the pixel distribution of the exposure accurately represented the canopy structure. Known uncertainty sources include georeference errors (Frazer et al., 2000), the RGB light threshold used to partition the digital image into binary pixel elements (Cescatti, 2007; Jonckheere et al., 2005), nonlinear hemispherical lens distortion (Swaninathan et al., 2003), the solar position algorithm used to sample the hemispherical sky region corresponding to the sun position at a given time (Reda & Andreas, 2004), and height differences between the camera lens and the reference height used to evaluate the photo results with measurements or another model. In particular, biases in canopy gap fraction and LAI are known to result from the image threshold specification by over- or under-representing canopy coverage (Cescatti, 2007). Conversely, the other error sources mentioned above are generally more random in nature when evaluated over many photo locations and different canopy conditions. In all cases, care was taken to minimize the uncertainty values from the various sources (see Musselman et al., 2012b).

The overall significant underestimation of cumulative irradiance by the Beer's-type model could be explained by potential errors in the primary model parameter LAI or in the parameters of the canopy shading factor such as the mean measured canopy height and diameter. Underestimation could also be a result of model structural errors such as the assumption of a spherical leaf distribution specified within the estimate of the canopy extinction coefficient k (Tarboton & Luce, 1996) (see Appendix A). Improved results could be obtained by calibrating the Beer's-type model to determine the stand-specific k value and treating the solar elevation within a cosine approximation applied to Eq. (A2) as Chen et al. (1997b), but the results would not improve simulated spatial patterns. More realistic spatial patterns of the Beer's-type model might be possible by introducing directionality in the estimation of canopy metrics.

The LiDAR-derived canopy transmittance estimates are based on the assumption that the pulse returns correctly sample all canopy elements that influence solar beam transmission. Chasmer et al. (2006) identified a systematic bias of airborne LiDAR returns toward the top of the canopy with less penetration to a depth where the largest biomass is typically found. The result of this canopy occlusion would be an under-representation of canopy structure and a positive bias in the raytrace transmittance estimate. Using simple trigonometry and knowledge of the (x, y, z) positions of the sensor and pulse return, Hagstrom et al. (2010) explicitly identified the number and location of voxels that went unsampled as a result of pulse occlusion. The authors advised that data users request that flight position be recorded for

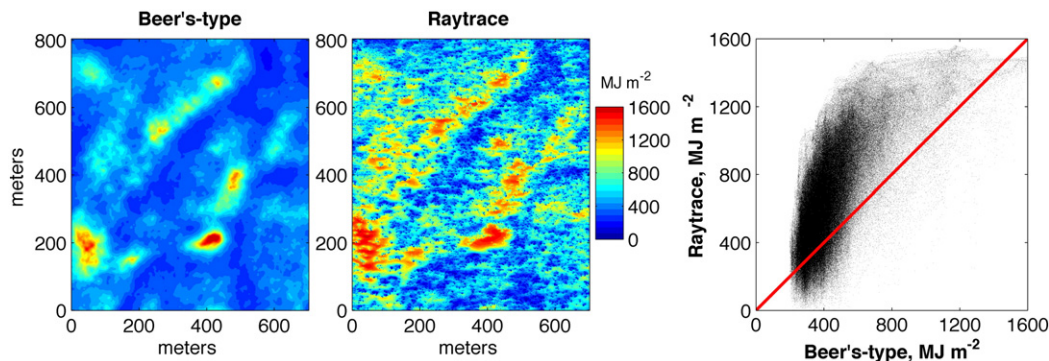


Fig. 11. The cumulative sub-canopy direct beam solar irradiance integrated between 01 March and 21 June 2010 as estimated by the Beer's-type (left) and the ray-tracing (center) transmittance models. Units are in mega-Joules per square meter (MJ m⁻²). The scatterplot (right) illustrates the relative per pixel cumulative irradiance predicted by the two models. The 1:1 line is shown.

each pulse. With this information, Hagstrom and Messinger (2011) was able to quantify uncertainty in the related 3-D voxel model. Sensor platform position was not provided in the 2010 NCALM dataset, but its utility in uncertainty characterization should be evaluated in future raytrace studies. The combination of multiple flight datasets and the use of all pulse returns may have reduced the potential bias by increasing the sample density of the 3-D canopy space. Furthermore, the sparse nature of the red fir tree distribution (Fig. 1) would be expected to result in less occlusion of lower canopy elements relative to a denser forest canopy with fewer gaps. Regardless, occlusion of lower canopy elements by the upper canopy is likely the primary source of uncertainty and bias with implications both on the estimation of LPI used to predict LAI' and the voxel-based raytrace model used to estimate transmittance.

The secondary source of uncertainty and one that plagues many studies that attempt to relate ground-based measurements to LiDAR metrics is spatial co-registration between LiDAR samples and field measurement locations (Hopkinson & Chasmer, 2009). The horizontal accuracy of GPS units used to record photo locations was between 1 and 2 m after differential correction. These errors would act to weaken the regression equations used to estimate LAI' from LPI (Frazer et al., 2011; Gobakken & Næsset, 2009; Patterson & Williams, 2003) and increase the errors between point-scale canopy transmittance estimates from photo and LiDAR.

6.7. Future directions

The topic of airborne LiDAR occlusion requires more work. Particularly, it is not clear how the presented work will apply to very dense forest environments characterized by closed canopies where canopy penetration would be limited. It is possible that such environments would closer approximate the underlying assumptions of the Beer's-type models. In general, the assumptions inherent to a Beer's-type model do not apply in heterogeneous canopy conditions, particularly at the high spatial resolution offered by LiDAR. At these scales, geometric shading modifications lack physical basis when provided static canopy metrics (e.g. gap fraction, canopy height, and LAI') that lack directionality in azimuth and zenith directions for the estimation of solar beam canopy transmittance. The results are shown to be inconsistent with those obtained from ground-based and raytrace estimates. A parsimonious modification to a Beer's-type model is warranted. Particularly, improvements to a Beer's-type estimate of solar beam canopy transmittance may be possible with a dynamic measurement of canopy height and openness that averages the metrics over the general spatial region that influences the solar beam transmittance. In this way, the canopy structure metrics would exhibit temporal and spatial variability that leverages the canopy structure detail available from LiDAR and results in a more physically based estimate of solar beam transmittance without the computational expense of a raytrace model.

The accuracy of snowmelt models is most limited in forested areas due to a host of challenges related to characterizing the influence of vegetation structure on sub-canopy mass and energy fluxes (Rutter et al., 2009). It is shown that a high-resolution raytrace model can greatly improve spatially explicit characterization of shortwave forcing compared to a distributed application of a Beer's-type transmittance model. The results could be used to improve snowmelt model accuracy, which can lead to improved predictions of hydrological processes and ecohydrologic response to vegetation and climate change. In addition, the technique could be used in studies of forest litter and soil heating (e.g. Baldocchi et al., 2000) and stream temperature (e.g. Brown & Krygier, 1970; Johnson & Jones, 2000) to evaluate the partition and exchange of energy within forest ecosystems and to better understand the associated spatiotemporal patterns.

7. Conclusions

When compared to point-scale explicit estimates from a single hemispherical photo location, the raytrace model resolved the complex seasonal and diurnal variability of solar direct beam canopy transmittance resulting from individual trees. The more conceptual Beer's-type model could not attain the same level of detail. The normalized mean absolute error values of the raytrace model were nearly 50% lower than the Beer's-type model from early May through 21 June. Unlike the raytrace model, the Beer's-type model was generally unable to simulate the complex irradiance patterns associated with individual trees, clustering of trees and gaps, and the periphery of gaps and large clearings. The Beer's-type model errors were highest precisely when accurate estimates of radiation are most important for snowmelt (i.e., the spring melt season). The results confirm known limitations of Beer's-type canopy transmittance models while highlighting the utility of the raytrace model to explicitly resolve the influence of heterogeneous canopy structure on direct beam transmissivity. The Beer's-type model estimated a mean cumulative irradiance over the snowmelt season (i.e. 01 March–21 June) of 428 MJ m^{-2} while the raytrace model estimated 631 MJ m^{-2} ; a 32% average underestimation by the Beer's-type model. The raytrace model is shown to capture a high level of variability necessary to simulate explicit plot- and stand-scale solar irradiance patterns known to govern snowmelt dynamics and soil water availability. The improved characterization of sub-canopy solar radiation has implications for understanding the sensitivity of snowmelt timing and magnitude to changes in climate and land cover.

Acknowledgments

Funding for this work was provided in part by National Science Foundation grants EAR-071160, EAR-1032295, EAR-1032308, EAR-1141764, the Southern Sierra Critical Zone Observatory (EAR-0725097), a Major Research Instrumentation grant (EAR-0619947), the Mountain Research Initiative, NASA grant NNX11AK35G and a NASA Earth System Science Fellowship. The authors thank J. Pomeroy for his constructive feedback on an early version of the manuscript, P. Kirchner and R. Bales for field support, and three anonymous reviewers for valuable input that greatly improved the paper.

Appendix A. Beer's-type model description

Solar radiation beneath the forest canopy $R_{S \downarrow, subdir}$ is traditionally estimated with a multiplicative reduction of above-canopy solar radiation $R_{S \downarrow, dir}$ using an estimate of the forest canopy transmittance, τ .

$$R_{S \downarrow, subdir} = \tau R_{S \downarrow, dir} \quad (A1)$$

The canopy transmittance is commonly estimated with a two-parameter application of the Beer-Lambert law (Monsi & Saeki, 1953), which assumes an exponential reduction of $R_{S \downarrow, dir}$. Hellström (2000) reported this relationship as:

$$\tau_i = \exp(-kLAI') \quad (A2)$$

where LAI' is the effective leaf area index and k is a vegetation-dependent attenuation coefficient assuming a horizontal leaf angle distribution (Liston & Elder, 2006). Tarboton and Luce (1996) used a similar formulation but assumed a spherical leaf angle distribution

and defined k as a function of the solar zenith angle θ as in Campbell and Norman (1989),

$$k = \frac{1}{2 \cos(\theta)} \quad (\text{A3})$$

Eq. (A3) permits increased (reduced) canopy transmission of solar radiation when the sun is higher (lower) in the sky and the canopy path length of the direct solar beam is shorter (longer). Eqs. (A2) and (A3) treat the canopy as a homogeneous medium. In many cases, however, canopy gaps can have profound impacts on the magnitude and the spatiotemporal variability of sub-canopy net radiation. Liston and Elder (2006) accounts for the case that canopy gaps permit an additive fraction of solar radiation to pass unimpeded to the forest floor as

$$\tau = \tau_i f_c + (1 - f_c) \quad (\text{A4})$$

where f_c is the fraction of forest cover (note that Liston and Elder (2006) presented Eq. (A4) in terms of canopy gap fraction) and τ on the left hand side is the new transmittance that accounts for both partial canopy transmission and full gap transmission. Eq. (A4) effectively assumes that the sun is directly overhead in regard to the additive contribution of solar transmission through canopy gaps. Far more often, however, solar zenith angles result in shade being cast by trees into canopy gaps causing an apparent reduction of the canopy gap fraction from the perspective of the solar beam (Gryning et al., 2001). A geometric canopy shading factor f_{sh} was introduced by Gryning et al. (2001) that treats the ground as fully shaded when $f_{sh} = 1$ and the shade to be directly under the tree canopies when $f_{sh} = f_c$, which only happens when the sun is at zenith. For consistency, the shade factor of Gryning et al. (2001) is referred to hereafter as the apparent forest cover fraction f_{ac} where $f_c \leq f_{ac} \leq 1$ and was computed as described below. The reader is referred to Gryning et al. (2001) for the derivation.

The critical solar elevation angle α_c below which the canopy gaps are fully shaded and $f_{ac} = 1$ was estimated as

$$\tan \alpha_c = \frac{4h}{\pi d} \left(\frac{f_c}{1 - f_c} \right) \quad (\text{A5})$$

where h and d are the average tree height and canopy diameter, respectively (Gryning et al., 2001). Mean tree height and canopy diameter within the domain were determined from the LiDAR data. When the solar elevation angle α exceeded the critical elevation angle α_c , f_{ac} was estimated as Gryning et al. (2001) as

$$f_{ac} = f_c \left(1 + \frac{4h}{\pi d \tan \alpha} \right) \quad \alpha \geq \alpha_c \quad (\text{A6})$$

Eq. (A4) was then modified to replace the canopy cover fraction f_c with the apparent canopy cover fraction f_{ac} to account for reduced canopy transmittance resulting from shade cast on ground area that would otherwise be considered a canopy gap. The solar zenith angle required in Eq. (A3) was estimated as in Reda and Andreas (2004) at five-minute time steps for all days between the winter and summer solstices.

Appendix B. LAI' from hemispherical photos

Hemispherical photos were used to estimate LAI' using Miller's (1967) theorem of canopy gap fraction. The metric *gap fraction* refers

to the gap frequency (i.e., the likelihood of an infinitesimal beam penetrating the canopy in a given direction (Ross, 1981)) integrated over a specified hemispherical sky area (Weiss et al., 2004).

$$LAI' = 2 \int_0^{\pi/2} \ln \left[\frac{1}{P(\theta)} \right] \cos \theta \sin \theta d\theta \quad (\text{B1})$$

In Eq. (B1), $P(\theta)$ is the gap fraction at the zenith view angle θ . The gap fraction at a given zenith angle can be calculated from a hemispherical photo as in Campbell and Norman (1989) as

$$P(\theta) = \exp \left(- \frac{G(\theta) LAI'}{\cos \theta} \right) \quad (\text{B2})$$

where $G(\theta)$ is a projection coefficient corresponding to the fraction of foliage projected on a plane normal to the zenith angle (Chen et al., 1997a). Using multiple angle measurements of $P(\theta)$, $G(\theta)$ and LAI' were computed simultaneously. Five measurements of $P(\theta)$ were made over the zenith to 75° θ range in 15° increments. The iterative procedure was used to estimate LAI' at the locations of the 24 hemispherical photos. The photo-derived LAI' values were used in Eqs. (A2) and (A1) to estimate the Beer's-type canopy transmittance at photo locations.

References

- Allen, R. G., Trezza, R., & Tasumi, M. (2006). Analytical integrated functions for daily solar radiation on slopes. *Agricultural and Forest Meteorology*, 139(1–2), 55–73.
- Amanatides, J., & Woo, A. (1987). *A fast voxel traversal algorithm for ray tracing, paper presented at Eurographics*. New York: Elsevier.
- ASPRS (2012). *LAS 1.4 R12 Format Specification, Data format documentation created by the LiDAR sub-committee of the American Society for Photogrammetry and Remote Sensing (ASPRS)*. (Available online: http://www.asprs.org/a/society/committees/standards/LAS_1_4_r12.pdf. 27 pp. Last accessed on September 19th, 2012).
- Baldocchi, D. D., Law, B. E., & Anthoni, P. M. (2000). On measuring and modeling energy fluxes above the floor of a homogeneous and heterogeneous conifer forest. *Agricultural and Forest Meteorology*, 102(2), 187–206.
- Bales, R. C., Molotch, N. P., Painter, T. H., Dettinger, M. D., Rice, R., & Dozier, J. (2006). Mountain hydrology of the western United States. *Water Resources Research*, 42(8), W08432.
- Barilotti, A., Turco, S., & Alberti, G. (2006). LAI determination in forestry ecosystems by LiDAR data analysis. *Paper presented at Workshop on 3D Remote Sensing in Forestry, BOKU Vienna, 14-15/02/2006*.
- Black, T. A., Chen, J. M., Lee, X., & Sagar, R. M. (1991). Characteristics of shortwave and longwave irradiances under a Douglas-fir forest stand. *Canadian Journal of Forest Research*, 21(7), 1020–1028.
- Brown, G. W., & Krygier, J. T. (1970). Effects of clear-cutting on stream temperature. *Water Resources Research*, 6(4), 1133–1139.
- Byram, G. M., & Jemison, G. M. (1943). *Solar radiation and forest fuel moisture*. Washington, DC: United State Government Printing Office.
- Campbell, G. S., & Norman, J. M. (1989). Plant physiological ecology field methods and instrumentation. In G. Russell, B. Marshall, & P. G. Jarvis (Eds.), *Canopy structure* (pp. 301–325). London: Chapman and Hall.
- Cescatti, A. (2007). Indirect estimates of canopy gap fraction based on the linear conversion of hemispherical photographs: Methodology and comparison with standard thresholding techniques. *Agricultural and Forest Meteorology*, 143(1, Åi2), 1–12.
- Chasmer, L., Hopkinson, C., & Treitz, P. (2006). Investigating laser pulse penetration through a conifer canopy by integrating airborne and terrestrial lidar. *Canadian Journal of Remote Sensing*, 32, 116–125.
- Chen, J. M., Plummer, P. S., Rich, M., Gower, S. T., & Norman, J. M. (1997a). Leaf area index of boreal forests: Theory, techniques, and measurements. *Journal of Geophysical Research*, 102(D24), 29,429–429,443.
- Chen, J. M., Blanken, P. D., Black, T. A., Guilbeault, M., & Chen, S. (1997b). Radiation regime and canopy architecture in a boreal aspen forest. *Agricultural and Forest Meteorology*, 86(1–2), 107–125.
- Cho, H. -C., Slatton, K. C., Cheung, S., & Hwang, S. (2011). Stream detection for LiDAR digital elevation models from a forested area. *International Journal of Remote Sensing*, 32(16), 4695–4721.
- Corona, P., Cartisano, R., Salvati, R., Chirici, G., Floris, A., Di Martino, P., et al. (2012). Airborne Laser Scanning to support forest resource management under alpine, temperate and Mediterranean environments in Italy. *European Journal of Remote Sensing*, 45, 27–37.
- Ellis, C. R., & Pomeroy, J. W. (2007). Estimating sub-canopy shortwave irradiance to melting snow on forested slopes. *Hydrological Processes*, 21(19), 2581–2593.
- Essery, R., Bunting, P., Hardy, J., Link, T., Marks, D., Melloh, R., et al. (2008). Radiative transfer modeling of a coniferous canopy characterized by airborne remote sensing. *Journal of Hydrometeorology*, 9, 228–241.

- Frazer, G. W., Canham, C. D., & Lertzman, K. P. (1999). *Gap Light Analyser (GLA)*. Version 2.0: Imaging Software to Extract Canopy Structure and Gap Light Transmission Indices From True-Colour Fisheye Photographs. Users Manual and Program Documentation. Millbrook, New York: Simon Fraser University, Burnaby, B.C. and the Institute of Ecosystem Studies.
- Frazer, G. W., Magnussen, S., Wulder, M. A., & Niemann, K. O. (2011). Simulated impact of sample plot size and co-registration error on the accuracy and uncertainty of LiDAR-derived estimates of forest stand biomass. *Remote Sensing of Environment*, 115(2), 636–649.
- Frazer, G. W., Trofymow, J. A., & Lertzman, K. P. (2000). Canopy openness and leaf area in chronosequences of coastal temperate rainforests. *Canadian Journal of Forest Research*, 30(2), 239–256.
- Gay, L., Knoerr, K., & Braaten, M. (1971). Solar radiation variability on the floor of a pine plantation. *Agricultural Meteorology*, 8, 39–50.
- Gobakken, T. G. T., & Næsset, E. N. E. (2009). Assessing effects of positioning errors and sample plot size on biophysical stand properties derived from airborne laser scanner data. *Canadian Journal of Forest Research*, 39(5), 1036–1052.
- Golding, D. L., & Swanson, R. H. (1978). Snow accumulation and melt in small forest openings in Alberta. *Canadian Journal of Forest Research*, 8(4), 380–388.
- Gray, H. R. (1956). *The form and taper of forest-tree stems*. Imperial Forestry Institute, University of Oxford.
- Gray, D., & Male, D. (1981). *Handbook of snow: Principles, processes*. Management and Use. Oxford: Pergamon.
- Gryning, S. E., Batchvarova, E., & DeBruin, H. A. R. (2001). Energy balance of a sparse coniferous high-latitude forest under winter conditions. *Boundary-Layer Meteorology*, 99, 465–488.
- Hagstrom, S., & Messinger, D. (2011, June 01). Line-of-sight analysis using voxelized discrete lidar. *Proc. SPIE 8037, Laser Radar Technology and Applications XVI*, 80370B, <http://dx.doi.org/10.1117/12.884049>.
- Hagstrom, S., & Messinger, D. (2012, May 1). Line-of-sight measurement in large urban areas using voxelized lidar. *Proc. SPIE 8379, Laser Radar Technology and Applications XVII*, 837907, <http://dx.doi.org/10.1117/12.918697>.
- Hagstrom, S., Messinger, D., & Brown, S. (2010). *Feature extraction using voxel aggregation of focused discrete lidar data*. Orlando, Florida, USA: SPIE.
- Helbig, N., Löwe, H., & Lehning, M. (2009). Radiosity approach for the shortwave surface radiation balance in complex terrain. *Journal of the Atmospheric Sciences*, 66(9), 2900–2912.
- Hellström, R.Å. (2000). Forest cover algorithms for estimating meteorological forcing in a numerical snow model. *Hydrological Processes*, 14(18), 3239–3256.
- Hopkinson, C., & Chasmer, L. (2009). Testing LiDAR models of fractional cover across multiple forest ecozones. *Remote Sensing of Environment*, 113(1), 275–288.
- Johnson, S. L., & Jones, J. A. (2000). Stream temperature responses to forest harvest and debris flows in western Cascades, Oregon. *Canadian Journal of Fisheries and Aquatic Sciences*, 57(S2), 30–39.
- Jonckheere, I., Nackaerts, K., Muys, B., & Coppin, P. (2005). Assessment of automatic gap fraction estimation of forests from digital hemispherical photography. *Agricultural and Forest Meteorology*, 132(1), 96–114.
- Korhonen, L., Korpela, I., Heiskanen, J., & Maltamo, M. (2011). Airborne discrete-return LIDAR data in the estimation of vertical canopy cover, angular canopy closure and leaf area index. *Remote Sensing of Environment*, 115(4), 1065–1080.
- Kraus, K., & Pfeifer, N. (1998). Determination of terrain models in wooded areas with airborne laser scanner data. *ISPRS Journal of Photogrammetry and Remote Sensing*, 53(4), 193–203.
- Lefsky, M. A., Cohen, W. B., Acker, S. A., Parker, G. G., Spies, T. A., & Harding, D. (1999). Lidar remote sensing of the canopy structure and biophysical properties of Douglas-fir western hemlock forests. *Remote Sensing of Environment*, 70(3), 339–361.
- Liston, G. E., & Elder, K. (2006). A distributed snow-evolution modeling system (snowmodel). *Journal of Hydrometeorology*, 7(6), 1259–1276.
- Lovell, J., Jupp, D., Culvenor, D., & Coops, N. (2003). Using airborne and ground-based ranging lidar to measure canopy structure in Australian forests. *Canadian Journal of Remote Sensing*, 29(5), 607–622.
- Marsh, C. B., Pomeroy, J. W., & Spiteri, R. J. (2012). Implications of mountain shading on calculating energy for snowmelt using unstructured triangular meshes. *Hydrological Processes*, 26(12), 1767–1778.
- Miller, J. B. (1967). A formula for average foliage density. *Australian Journal of Botany*, 15, 141–144.
- Molotch, N. P., & Margulis, S. A. (2008). Estimating the distribution of snow water equivalent using remotely sensed snow cover data and a spatially distributed snowmelt model: A multi-resolution, multi-sensor comparison. *Advances in Water Resources*, 31(11), 1503–1514.
- Monsi, M., & Saeki, T. (1953). Über den Lichtfaktor in den Pflanzengesellschaften und seine Bedeutung für die Stoffproduktion. *Japanese Journal of Botany*, 14, 22–52.
- Morsdorf, F., Koetz, B., Meier, E., Itten, K., & Allgöwer, B. (2006). Estimation of LAI and fractional cover from small footprint airborne laser scanning data based on gap fraction. *Remote Sensing of Environment*, 104(1), 50–61.
- Musselman, K. N., Molotch, N. P., Margulis, S. A., Lehning, M., & Gustafsson, D. (2012a). Improved snowmelt simulations with a canopy model forced with photo-derived direct beam canopy transmissivity. *Water Resources Research*, 48(10).
- Musselman, K. N., Molotch, N. P., Margulis, S. A., Kirchner, P., & Bales, R. C. (2012b). Influence of canopy structure and direct beam solar irradiance on snowmelt rates in a mixed conifer forest. *Agricultural and Forest Meteorology*, 161C, 46–56.
- NCALM (2012). edited, p. Online. <http://www.ncalm.cive.uh.edu/home/instruments/ncalm.html> (Accessed 9/20/12).
- Nijssen, B., & Lettenmaier, D. P. (1999). A simplified approach for predicting shortwave radiation transfer through boreal forest canopies. *Journal of Geophysical Research*, 104(D22), 27859–27868.
- Parker, G. G., Lefsky, M. A., & Harding, D. J. (2001). Light transmittance in forest canopies determined using airborne laser altimetry and in-canopy quantum measurements. *Remote Sensing of Environment*, 76(3), 298–309.
- Patterson, P. L., & Williams, M. S. (2003). Effects of registration error between remotely sensed and ground data on estimators of forest area. *Forest Science*, 49(1), 110–118.
- Pinty, B., et al. (2004). Radiation Transfer Model Intercomparison (RAMI) exercise: Results from the second phase. *Journal of Geophysical Research*, 109(D6), D06210.
- Pomeroy, J. W., Ellis, C., Rowlands, A., Essery, R., Hardy, J., Link, T., et al. (2008). Spatial variability of shortwave irradiance for snowmelt in forests. *Journal of Hydrometeorology*, 9(6), 1482–1490.
- Popescu, S. C., & Zhao, K. (2008). A voxel-based lidar method for estimating crown base height for deciduous and pine trees. *Remote Sensing of Environment*, 112(3), 767–781.
- Pysalo, U., Oksanen, J., & Sarjakoski, T. (2009). Viewshed analysis and visualization of landscape voxel models. *Paper presented at 24th International Cartographic Conference, Santiago, Chile*.
- Raleigh, M. S., Rittger, K., Moore, C. E., Henn, B., Lutz, J. A., & Lundquist, J. D. (2013). Ground-based testing of MODIS fractional snow cover in subalpine meadows and forests of the Sierra Nevada. *Remote Sensing of Environment*, 128, 44–57.
- Reda, I., & Andreas, A. (2004). Solar position algorithm for solar radiation applications. *Solar Energy*, 76(5), 577–589.
- Reifsnyder, W. E., Furnival, G. M., & Horowitz, J. L. (1971). Spatial and temporal distribution of solar radiation beneath forest canopies. *Agricultural Meteorology*, 9, 21–37.
- Ross, J. K. (Ed.). (1981). *The radiation regime and architecture of plant stands*. The Hague and Boston and Hingham, Mass.: Dr. W. Junk Publishers (392 pp.).
- Rutter, N., et al. (2009). Evaluation of forest snow processes models (SnowMIP2). *Journal of Geophysical Research-Atmospheres*, 114.
- Swaninathan, R., Grossberg, M. D., & Nayar, S. K. (2003). A perspective on distortions, paper presented at Computer Vision and Pattern Recognition, 2003. *Proceedings. 2003 IEEE Computer Society Conference on, IEEE*.
- Tarboton, D. G., & Luce, C. H. (1996). *Utah Energy Balance Snow Accumulation and Melt Model (UEB)*.
- Todd, K., Csillag, F., & Atkinson, P. M. (2003). Three-dimensional mapping of light transmittance and foliage distribution using lidar. *Canadian Journal of Remote Sensing*, 29(5), 544–555.
- Varhola, A., Frazer, G., Teti, P., & Coops, N. (2012). Estimation of forest structure metrics relevant to hydrologic modeling using coordinate transformation of airborne laser scanning data. *Hydrology and Earth System Sciences Discussions*, 9, 5531–5573.
- Weiss, M., Baret, F., Smith, G., Jonckheere, I., & Coppin, P. (2004). Review of methods for in situ leaf area index (LAI) determination: Part II. Estimation of LAI, errors and sampling. *Agricultural and Forest Meteorology*, 121(1), 37–53.